ELECTROCHEMICAL SCIENCES

Ultrastable atomic copper nanosheets for selective electrochemical reduction of carbon dioxide

Lei Dai,[1] Qing Qin,[1] Pei Wang,[1] Xiaojing Zhao,[1] Chengyi Hu,[1] Pengxin Liu,[1] Ruixuan Qin,[1] Mei Chen,[1] Daohui Ou,[2] Chaofa Xu,[1] Shiguang Mo,[1] Binghui Wu,[1] Gang Fu,[1] Peng Zhang,[3] Nanfeng Zheng[1]*

The electrochemical conversion of CO_2 and H_2O into syngas using renewably generated electricity is an attractive approach to simultaneously achieve chemical fixation of CO_2 and storage of renewable energy. Developing cost-effective catalysts for selective electroreduction of CO_2 into CO is essential to the practical applications of the approach. We report a simple synthetic strategy for the preparation of ultrathin $Cu/Ni(OH)_2$ nanosheets as an excellent cost-effective catalyst for the electrochemical conversion of CO_2 and H_2O into tunable syngas under low overpotentials. These hybrid nanosheets with Cu(0)-enriched surface behave like noble metal nanocatalysts in both air stability and catalysis. Uniquely, Cu(0) within the nanosheets is stable against air oxidation for months because of the presence of formate on their surface. With the presence of atomically thick ultrastable Cu nanosheets, the hybrid $Cu/Ni(OH)_2$ nanosheets display both excellent activity and selectivity in the electroreduction of CO_2 to CO. At a low overpotential of 0.39 V, the nanosheets provide a current density of 4.3 mA/cm^2 with a CO faradaic efficiency of 92%. No decay in the current is observed for more than 22 hours. The catalysts developed in this work are promising for building low-cost CO_2 electrolyzers to produce CO.

INTRODUCTION

Syngas, as a mixture of primarily hydrogen and carbon monoxide, is an extremely important raw material for many large-scale chemical industries such as production of hydrogen, ammonia, and hydrocarbon fuels (1–4). Currently, syngas is mainly produced from hydrocarbon feedstock (for example, natural gas, coal, biomass) through conventional processes, such as steam reforming, dry reforming with CO_2, or partial oxidation by O_2 (5–8). However, most of these methods are typically carried out at high temperatures with the help of catalysts (8). With the increasing demand of energy production while minimizing environmental impact, the production of syngas from CO_2 and water at room temperature, using electricity generated from renewable energy sources, has recently received increasing research attention (9–12).

During the decades, significant research progress has been made on identifying cost-effective catalysts for CO_2 electroreduction to valuable fuels and chemicals (9–26). Different types of promising catalysts have been investigated, including homogeneous catalysts based on molecular metal complexes (14), heterogeneous catalysts based on metal-organic frameworks (15), and various nanomaterials such as AuCu nanoparticles (10), Au nanoparticles (27), nanoporous Ag (11), Co/Co$_3$O$_4$ hybrid nanosheets (16), Cu nanoparticles/nanowires (17–23), nanostructured Sn (24, 25), and transition metal dichalcogenides (26). Among these catalysts, owing to its natural abundance, Cu has been emerging as one of the most attractive and powerful elements for creating cost-effective electrocatalysts for CO_2 reduction (9, 28). Cu-based homogeneous and heterogeneous catalysts are capable of yielding versatile products such

as CO, formate, CH$_3$OH, CH$_4$, and even C$_{2+}$ species (9). However, unlike noble metal catalysts (for example, Au, Ag) (10, 11, 27), product selectivity of Cu nanocatalysts is usually poor and depends on the particle size, shape, and surface modifications of these catalysts (17–23). Moreover, in general, Cu(0) nanomaterials are easily oxidized in air (29, 30), and oxidized Cu species are readily reduced to Cu(0) under reducing potentials as well. It is, thus, not surprising that catalytic activity and selectivity of Cu catalysts in CO_2 electroreduction often vary with preparation techniques.

We now report a simple synthetic strategy for creation of novel ultrathin hybrid $Cu/Ni(OH)_2$ nanosheets, with a Cu(0)-enriched surface, that are uniquely stable against air oxidation. The nanosheets are prepared by first forming $Ni(OH)_2$ nanosheets, followed by substitution of Ni^{2+} by Cu^{2+} to yield $Ni_{1-x}Cu_x(OH)_2$ nanosheets. In the presence of sodium formate, the Cu^{2+} species are then reduced to Cu_2O and eventually to Cu(0) to form ultrathin hybrid $Cu/Ni(OH)_2$ nanosheets with a thickness of less than 3 nm. The two-dimensional (2D) Cu domains within the nanosheets are atomically thick and surface-stabilized by formate. The surface formate layer protects the Cu(0) nanosheets from air oxidation, making them stable in air for months. These air-stable $Cu/Ni(OH)_2$ nanosheets exhibit an excellent catalytic performance in the selective electroreduction of CO_2 into CO only. Consequently, the use of $Cu/Ni(OH)_2$ nanosheets enables the direct production of tunable syngas from CO_2 and water by applying different reduction potentials in the range between −0.4 and −1.0 V [versus reversible hydrogen electrode (RHE)]. At −0.5 V with an overpotential of 0.39 V, the current density reaches 4.3 mA/cm^2 with a CO faradaic efficiency (FE) of 92%.

In a typical synthesis of the hybrid $Cu/Ni(OH)_2$ nanosheets, a mixed solution of NiCl$_2$, Cu(acac)$_2$, and HCOONa in N,N'-dimethylformamide (DMF) (see Materials and Methods for more details) was prepared in a glass pressure vessel. The vessel was heated from room temperature to 160°C in 30 min and kept at this temperature for 10 hours. The mixture was cooled down to room temperature, and the maroon products were collected by centrifugation and washed several times with water.

[1]Collaborative Innovation Center of Chemistry for Energy Materials, State Key Laboratory for Physical Chemistry of Solid Surfaces, Engineering Research Center for Nano-Preparation Technology of Fujian Province, National Engineering Laboratory for Green Chemical Productions of Alcohols, Ethers, and Esters, and Department of Chemistry, College of Chemistry and Chemical Engineering, Xiamen University, Xiamen 361005, P. R. China. [2]Pen-Tung Sah Institute of Micro-Nano Science and Technology, Xiamen University, Xiamen, Fujian 361005, China. [3]Department of Chemistry, Dalhousie University, Halifax, Nova Scotia B3H4R2, Canada.
*Corresponding author. Email: nfzheng@xmu.edu.cn
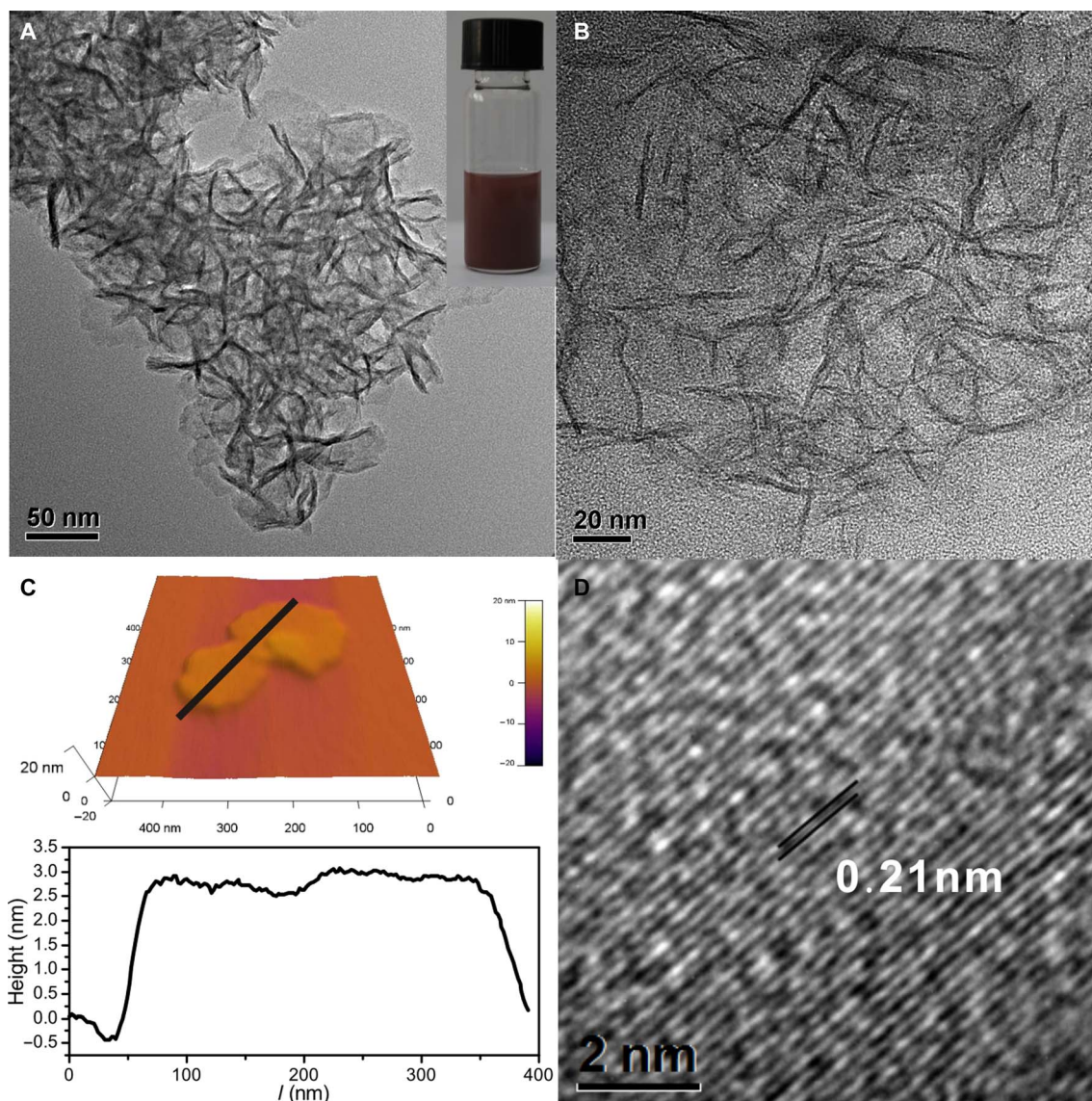
Fig. 1. Microscopic characterizations of the hybrid Cu/Ni(OH)₂ nanosheets. (**A**) Low-magnification TEM image. Inset: Photograph of a dispersion of the nanosheets in ethanol. (**B**) TEM image of the cross-sectional nanosheets obtained by microtoming. (**C**) AFM image (top) and the height profile (bottom) of the nanosheets. (**D**) HRTEM image of an individual nanosheet.

RESULTS

Low-magnification transmission electron microscopy (TEM) and scanning electron microscopy (SEM) images (Fig. 1A and fig. S1) revealed that the nanosheets were the dominant product. The nanosheets were interconnected to form highly porous architecture without being stacked together. Energy-dispersive x-ray spectroscopy (EDX) analysis showed that the nanosheets were composed of Ni and Cu elements with an atomic ratio of 59 and 41% (fig. S2), respectively, close to the Ni/Cu atomic ratio of 60:40 measured by inductively coupled plasma mass spectrometry (ICP-MS). To have a clear picture of their thickness, the nanosheets were embedded in epoxy resin, microtomed, and examined by TEM. A thickness of ~2.8 nm was observed by TEM (Fig. 1B), consistent with the number measured by atomic force microscopy (AFM) (Fig. 1C). Lattice fringes with an interplanar spacing of 0.21 nm, corresponding to the (111) fringe of Cu(0), were revealed

in the high-resolution TEM (HRTEM) image of an individual nanosheet on the TEM grid (Fig. 1D). The presence of strong diffraction (111) and (200) peaks was also verified by the selected-area electron diffraction pattern taken from the 3D-connected nanosheets (fig. S1, C and D), suggesting the good crystallinity of the nanosheets.

Curiously, despite the presence of a large content of Ni species, all x-ray diffraction (XRD) peaks of the obtained nanosheets are in good agreement with standard data [JCPDS (Joint Committee on Powder Diffraction Standards) #65-9743] on face-centered cubic (fcc) Cu (Fig. 2A). The maroon-colored product also showed a characteristic ultraviolet-visible (UV-vis) absorption spectrum (fig. S3). We attributed the obvious 595-nm absorption peak to a characteristic localized surface plasmon resonance absorption peak of the Cu(0) nanomaterials (30, 31). Although only metallic Cu was observed by HRTEM and XRD, the HAADF (high-angle annular dark-field)–TEM (scanning transmission
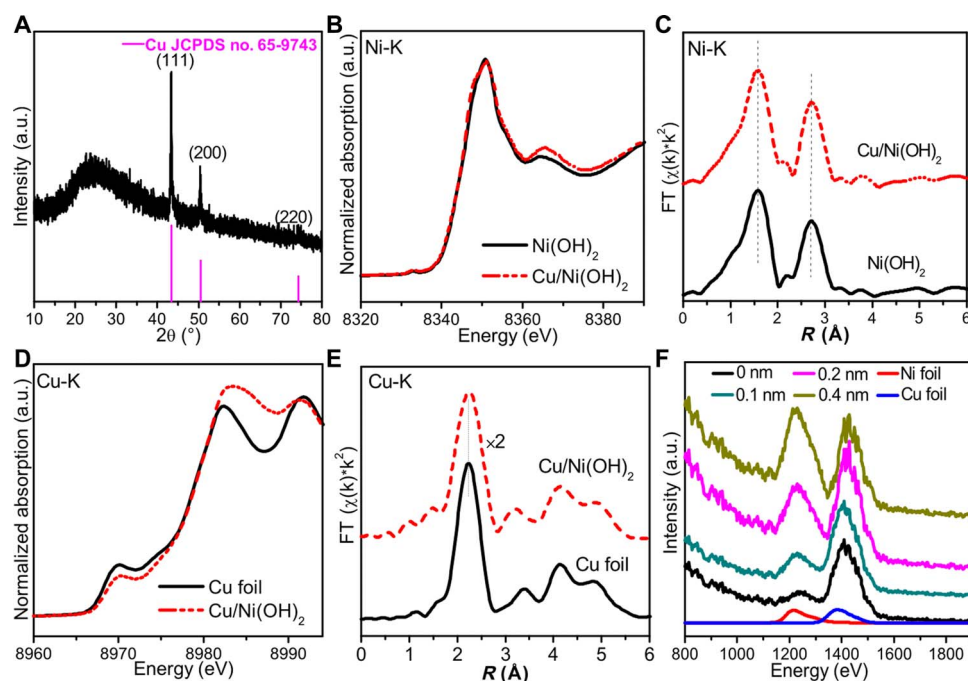
Fig. 2. Detailed structure characterizations of the Cu/Ni(OH)$_2$ nanosheets. (**A**) XRD pattern of the Cu/Ni(OH)$_2$ nanosheets. a.u., arbitrary units. (**B** to **E**) XANES and EXAFS fitting spectra of Cu/Ni(OH)$_2$ for Ni K-edge (B and C) and Cu K-edge (D and E). (**F**) HS-LEISS spectra for the nanosheets with different detected depths.

electron microscopy)–EDX mapping analysis showed that the element distributions of Ni and Cu overlapped nicely (fig. S4). So, the remaining question was: What were the Ni species in the nanosheets?

X-ray absorption spectroscopy (XAS) studies were carried out to evaluate both electronic states and local chemical environments of Ni and Cu in the obtained nanosheets. X-ray absorption near-edge structure (XANES) data suggested that Ni in the nanosheets was in the oxidation state of +2, similar to that of Ni(OH)$_2$, and that Cu had a metallic nature. The oxidation states revealed by XANES were consistent with x-ray photoelectron spectroscopy (XPS) results (fig. S5). Extended x-ray absorption fine structure (EXAFS) analysis of the Ni K-edge confirmed that the local atomic environment of Ni was identical to that of Ni(OH)$_2$ (Fig. 2, B and C), in which Ni is octahedrally coordinated by six oxygen atoms. Careful EXAFS analysis on Cu K-edge revealed a Cu–Cu bond distance of 2.54 Å, identical to that of Cu foil (Fig. 2, D and E). EXAFS fitting data also demonstrated that the coordination number of Cu was ~6, much smaller than that in Cu foil (fig. S6 and table S1), suggesting the ultrafine nature of Cu domains within the nanosheets. The appearance of 2NN (second nearest neighbor) Cu–Cu coordination around 3.3 Å and 3NN (third nearest neighbor) Cu–Cu around 4.1 Å, probably due to the Cu in nanosheets, has a 2D long-range ordered structure. We have built three structural models of Cu to simulate their Fourier transform (FT)–EXAFS using the FEFF 8 program: bulk Cu, one-atomic-layer Cu, and two-atomic-layer Cu. As shown in fig. S7, the 4.1 Å FT-EXAFS peak was present in the three structural models. However, the peak at ~3.3 Å would disappear when the Cu sheet has one atomic layer. However, if the Cu sheet has two atomic layers, then the 3.3 Å FT-EXAFS peak should be present. On the basis of the XPS spectra of the Cu/Ni(OH)$_2$ nanosheets (fig. S5, C and D), in the Cu 2p spectrum, the peaks are located at 955.3 eV (Cu 2p$_{1/2}$) and 932.6 eV (Cu 2p$_{3/2}$), and the Auger kinetic energy is 918.5 eV, indicating elemental Cu(0) (32). All these results confirmed

that the hybrid nanosheets were composed of both Ni(OH)$_2$ and metallic Cu nanosheets.

To further characterize the 3D distribution of Ni and Cu elements, we used high-sensitivity low-energy ion scattering spectroscopy (HS-LEISS) to detect the elements on the outermost atomic layer of the nanosheets. As shown in Fig. 2F, the peak intensity of Cu was much higher than Ni, suggesting the Cu-rich surface of the nanosheets. With increasing detected depth enabled by Ar ion sputtering, the relative intensity of Ni was increased. We thus proposed that the resulting hybrid Cu/Ni(OH)$_2$ nanosheets have a nanostructure with a Ni(OH)$_2$-rich core and a Cu(0)-rich surface. To confirm such a hybrid core-shell nanostructure, we also used a HCOOH/HCOONa mixture (pH 2.0) to selectively etch away Ni(OH)$_2$ from the hybrid nanosheets. It should be pointed out that the maroon color of the nanosheet dispersion was still well maintained after the 5-day etching process (fig. S8). However, as revealed by TEM (fig. S8, A and B), the original nanosheets with a larger diameter and thickness of ~3 nm are converted into very ill-defined nanosheets of atomic-scale thickness. ICP-MS data showed that the treatment etched away most Ni from the hybrid nanosheets. In the product collected after extensive etching, the atomic content of Ni was reduced to 8%, whereas the Cu content was increased to 92%. AFM analysis (fig. S8C) reveals an atomic thickness of 0.45 nm for the Cu nanosheets collected after the etching process. No peaks of CuO$_x$ or Ni(OH)$_2$ were detected in the XRD pattern (fig. S8D). XPS and Auger electron spectra revealed that Cu was still in the valence state of 0 (fig. S8E). All these results confirmed that the synthesized nanosheets had Cu(0) enriched on their surface.

To understand the formation process of the hybrid nanosheets, we investigated the products collected from the reaction at different times by TEM (fig. S9) and XRD (fig. S10). After the reaction temperature was increased from room temperature to 160°C in 30 min, the formation of blue-green colloidal dispersion was observed. The collected

product displayed only the XRD peaks of mixed $Ni(OH)_2$ and $Cu(OH)_2$. After being heated at 160°C for 1 and 3 hours, the mixture became brown-black, and the collected product displayed diffraction peaks of both $Ni(OH)_2$ and Cu_2O. When the heating time at 160°C was further extended to 5 and 15 hours, the color of the mixture became maroon, and the product mainly displayed diffraction peaks of Cu. The crystalline feature of the products was enhanced with the increasing heating time at 160°C. As revealed by ICP-MS measurements (fig. S11), the atomic content of Cu in the samples slightly increased from 9.2 to 42% as the heating time at 160°C increased from 0 to 15 hours. It should be noted that product composition depended strongly on reaction temperature. With all other conditions the same, lowering the temperature to 140°C yielded the $Cu_2O/Ni(OH)_2$ nanosheets. When the temperature was raised to 180°C, the formation of large Cu nanoparticles was observed (fig. S12).

On the basis of the above kinetic studies, the formation of the $Cu/Ni(OH)_2$ hybrid nanosheets was thus proposed as follows (Fig. 3): $Ni(OH)_2$ nanosheets were formed first temperature increased; next, Ni^{2+} was replaced by Cu^{2+}. This replacement process was driven by the K_{sp} (solubility product constant) of $Cu(OH)_2$ (5.6×10^{-20}), which was much smaller than that of $Ni(OH)_2$ (5.5×10^{-15}) and did not alter the nanosheets' thickness (fig. S13); this result was experimentally confirmed by reacting premade $Ni(OH)_2$ nanosheets (fig. S14A) with a mixture of $Cu(acac)_2$ and HCOONa. As shown in fig. S14B, there was no obvious change in nanosheet thickness after 19% Cu was added to $Ni(OH)_2$. The incorporated Cu^{2+} was enriched on the surface of the hybrid ultrathin $M(OH)_2$ nanosheets as suggested by LEISS (fig. S14C). With the presence of formate on their surface, $Cu(OH)_2$ domains within the nanosheets were readily reduced into Cu_2O and, eventually, Cu under the solvothermal condition. Because the whole reduction process took place within the nanosheets, the reduced Cu(0) species were confined as atomically thick sheets within the hybrid nanosheet framework. According to the proposed mechanism, both premade hexagonal β-$Ni(OH)_2$ and α-$Ni(OH)_2$ nanosheets were successfully applied as the templates for producing $Cu/Ni(OH)_2$ hybrid nanosheets by solvothermally treating them with a DMF solution of $Cu(acac)_2$ and HCOONa (figs. S15 and S16). It should be noted that, in the absence of any Ni precursor, only Cu(0) particles were obtained under the same reaction conditions even with extended reaction time (fig. S17).
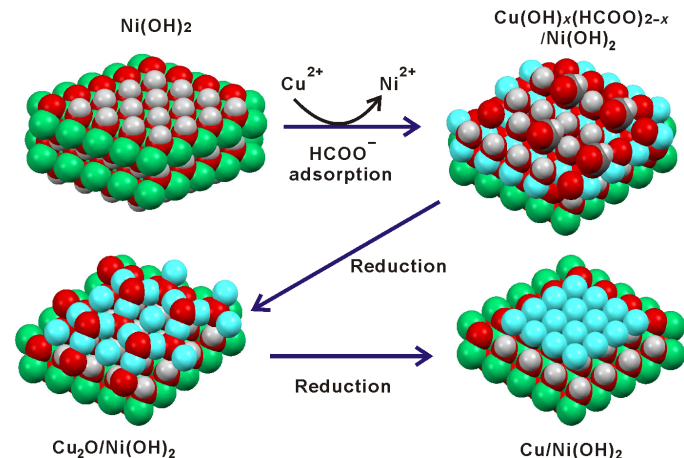
**Fig. 3. The proposed formation mechanism of the hybrid $Cu/Ni(OH)_2$ nanosheets.** Color codes: cyan, Cu; green, Ni; red, O; gray, C; white, H.

It is well documented that Cu nanomaterials have poor stability in air. To our surprise, Cu(0) within the $Cu/Ni(OH)_2$ nanosheets showed extreme stability against thermal treatment and air oxidation despite their atomic thickness. The ultrathin sheet-like feature of the hybrid nanosheets was well maintained after being heated at 280°C in N_2 for 3 hours (fig. S18). After being stored in ambient conditions for more than 3 months, XRD peaks of fcc Cu were still observed (Fig. 4, A and B). Both XPS and Auger electron spectra of Cu also verified that Cu in the air-stored Cu nanosheets was still in the valance state of 0 (fig. S19). More impressively, nanosheets baked at 100°C in air for 48 hours still displayed Cu(0) diffraction peaks without the appearance of peaks from its oxidation products (fig. S20). We attributed the excellent stability of the $Cu/Ni(OH)_2$ nanosheets to the presence of formate on their surface.

Temperature-programmed desorption/mass spectrometry (TPD-MS) measurements were first performed to detect the species released from the nanosheets upon heating in vacuum. A peak at a mass/charge ratio (m/z) of 45 confirmed the presence of $HCOO^-$ on the nanosheets (Fig. 4C). Elemental analysis (table S2) indicated a composition of 2.0% C and the N_2 adsorption-desorption isotherm at 77 K (fig. S21) revealed a BET (Brunauer-Emmett-Teller) surface area of 200 m^2/g. Estimated that the surface density of formate on the nanosheets was ~5 $HCOO^-$ per 1 nm^2. Moreover, as suggested by the strong infrared (IR) absorption band at around 1643 cm^{-1} (Fig. 4D), formate was adsorbed on the nanosheets mainly in a monodentate mode (33, 34).

Because of its lower redox potential than Cu, the protective layer of $HCOO^-$ can suppress oxidation of Cu through a mechanism similar to the cathodic protection in galvanized iron pipes. The protecting effect of $HCOO^-$ on Cu was easily visualized by observing the color change of the Cu foils before and after $HCOO^-$ modification. Simply treating the Cu foils with a solution of HCOONa readily prevented their surface from oxidation by air for months (fig. S22A). In our cyclovoltammetric studies, the Cu foil treated by $HCOO^-$ exhibited an oxidation peak at −0.15 V [versus saturated calomel electrode (SCE)] before the oxidation of Cu (fig. S22B). Although $HCOO^-$ is more easily oxidized than Cu, the slow oxidation kinetics of $HCOO^-$ helps to achieve the long-term stability of Cu in air. As expected, when $HCOO^-$ was replaced by CH_3COO^-, the nanosheets became more prone to air oxidation (figs. S23 and S24). No Cu nanosheets were obtained from the reaction without adding sodium formate (fig. S25). Therefore, in the synthesis $Cu/Ni(OH)_2$ nanosheets in this work, formate played three important roles: (i) as a base to precipitate out the $Ni(OH)_2$ nanosheets at the early stage of reaction, (ii) as a reducing agent to reduce $Cu(OH)_2$ domains into Cu_2O and finally Cu, and (iii) as a surface binding agent to protect Cu nanosheets from being oxidized.

Reforming CO_2 into fuels using electricity generated from renewable resources has attracted increasing attention during the past decades (9, 35, 36), and Cu-based materials have been emerging as promising cost-effective electrocatalysts for the CO_2 reduction (28). Motivated by the excellent stability and the high surface area of the hybrid $Cu/Ni(OH)_2$ nanosheets, we investigated their catalytic performance in the electrochemical reduction of CO_2. As shown in Fig. 5A, the nanosheets exhibited obvious responses to CO_2. The CO_2 reduction on the nanosheets had an onset potential of −0.37 V (versus RHE). In comparison, a much negative potential (−0.57 V) was required to initiate hydrogen evolution reaction (HER). At −0.5 V (versus RHE) with an overpotential (η) of 0.39 V, the current density of the hybrid $Cu/Ni(OH)_2$ nanosheets reached 4.3 mA/cm^2, much
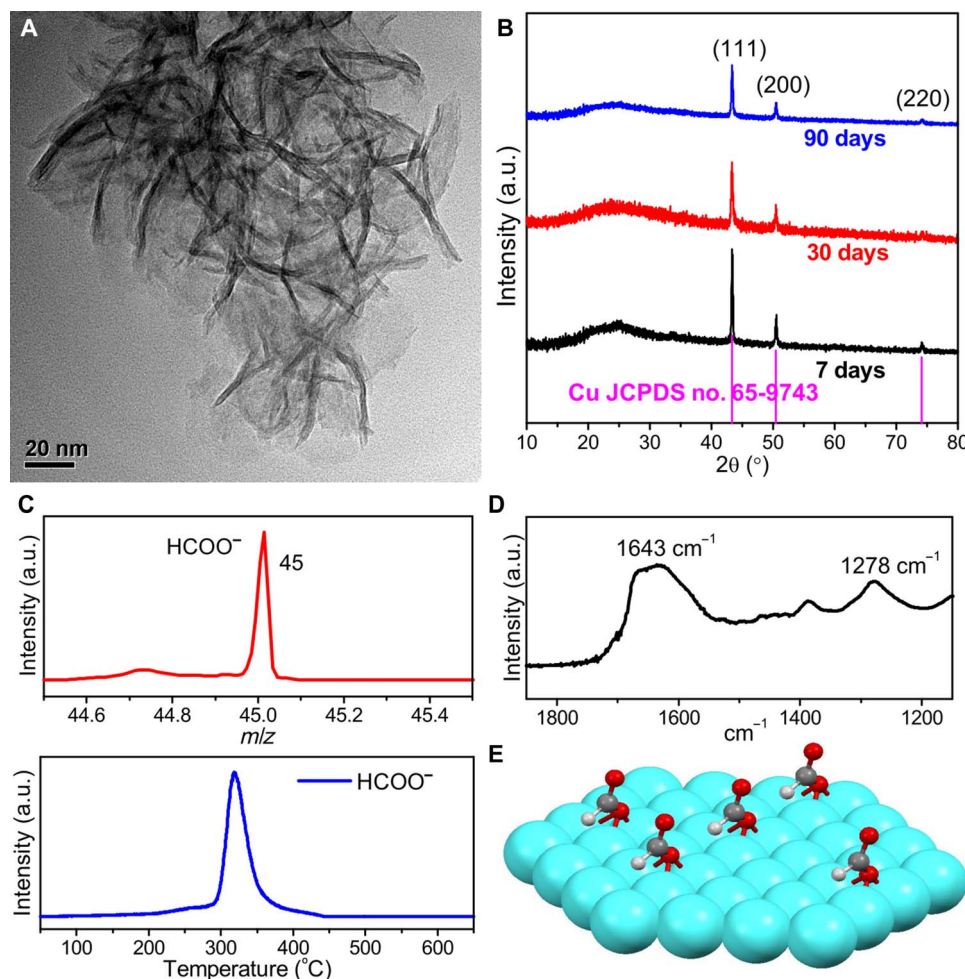
Fig. 4. Stability in air and surface species identification of the Cu/Ni(OH)$_2$ nanosheets. (A) TEM image of the Cu/Ni(OH)$_2$ nanosheets after being stored in air at room temperature for 90 days. (**B**) XRD patterns of the nanosheets after storing in air at room temperature for 7 to 90 days. (**C**) TPD-MS profiles of the Cu/Ni(OH)$_2$ nanosheets heated in vacuum. Whereas the bottom shows relative ionization intensities of the main decomposition products at different temperatures, the top displays the accumulative ionization intensity. m/z, mass/charge ratio. (**D**) FTIR spectrum of the nanosheets. (**E**) Adsorption model of formate on Cu. Color codes: cyan, Cu; red, O; gray, C; white, H.

higher than those of Cu nanoparticles (1.59 mA/cm^2) and Ni(OH)$_2$ nanosheets (fig. S26).

In the electroreduction of CO$_2$, selectivity is always a big issue because of the possible presence of complex reduction products (9). Although high selectivity of electrochemical CO$_2$ reduction has been recently achieved with various catalysts, for example, with noble metal catalysts (10, 11, 27), metal complex–based catalysts (15, 37), and Co-Co$_3$O$_4$ nanosheets (16), high catalytic selectivity has not been successfully achieved with Cu electrocatalysts at low overpotentials. The Cu/Ni(OH)$_2$ nanosheets in this study were found to be highly selective in reducing CO$_2$ to CO at low overpotentials. When applied potentials were between −0.4 and −1.0 V (versus RHE), no liquid products of CO$_2$ reduction were detected by ^{1}H nuclear magnetic resonance (NMR) (fig. S27). Only the syngas components H$_2$ and CO were produced. At a potential between −0.4 and −0.6 V (η = 0.29 to 0.49 V), the FE toward CO was above 40%, and the maximum FE of 92% was achieved at −0.5 V. When the potential was more negative than −0.6 V, HER became the dominant reaction (Fig. 5B). In comparison, the maximum FE of CO was only 25% at −0.5 V (fig. S26B). Ni(OH)$_2$ exhibited no activity in the CO$_2$ reduction with only H$_2$ detected (fig. S26C). It should be noted that the Ni(OH)$_2$ components in the hybrid Cu/Ni(OH)$_2$ nano-

sheets had no obvious contribution to the selectivity in the CO$_2$ reduction. The atomically thick Cu nanosheets obtained by etching Ni(OH)$_2$ from the hybrid nanosheets also exhibited high selectivity toward CO$_2$ to CO (fig. S28). At −0.5 V, the FE of CO was as high as 89%, only slightly smaller than that of Cu/Ni(OH)$_2$. Even at −0.6 V, the FE of CO was still as high as 75%. The hybrid Cu/Ni(OH)$_2$ nanosheets displayed excellent catalytic stability (Fig. 5C and fig. S29). In comparison, pure Cu nanosheets showed a poorer stability (fig. S26D). In the absence of Ni(OH)$_2$, Cu nanosheets were heavily sintered after the electrochemical catalysis (fig. S30). We thus attributed the excellent electrocatalytic stability of the Cu/Ni(OH)$_2$ nanosheets to the presence of both surface formates for stabilizing the metallic nature of Cu and Ni(OH)$_2$ as support for preventing Cu nanosheets from being sintered during electrocatalysis.

Volumetric CO$_2$ adsorption measurements demonstrated that both the hybrid Cu/Ni(OH)$_2$ nanosheets and the Cu nanosheets absorbed much more CO$_2$ than Cu nanoparticles, and Ni(OH)$_2$ nanosheets had almost no CO$_2$ adsorption (fig. S31). The high CO$_2$ adsorption capacity of the hybrid Cu/Ni(OH)$_2$ nanosheets well explains their catalytic activity. Furthermore, as revealed by the electrical impedance spectroscopy (fig. S32), the hybrid Cu/Ni(OH)$_2$ nanosheets exhibited a
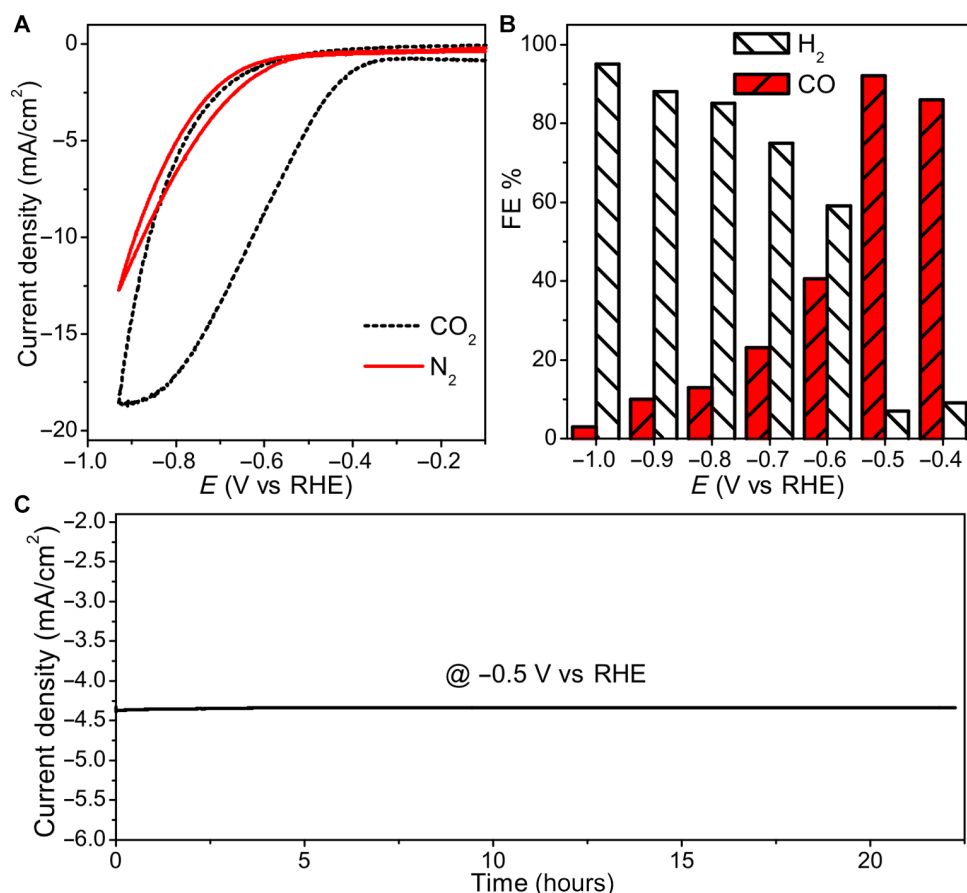
Fig. 5. Catalytic performances of the Cu/Ni(OH)₂ nanosheets in the electroreduction of CO₂. (**A**) Normalized polarization curves in N_2-saturated and CO_2-saturated 0.5 M $NaHCO_3$ aqueous solution by the electrode surface area of electrocatalysts. The scan rate was 10 mV/s. (**B**) FEs of CO and H_2 at different potentials. (**C**) Chronoamperometric current at −0.5 V versus RHE. The loading of the Cu/Ni(OH)₂ nanosheets on carbon paper was 0.5 mg/cm².

charge-transfer resistance of 24.2 ohms at the potential of −0.5 V, much smaller than those of Cu nanoparticles (63.4 ohms), Ni(OH)₂ nanosheets (85.6 ohms), and Cu nanosheets (39.7 ohms). This comparison indicated that the hybrid Cu/Ni(OH)₂ nanosheets exhibited a superior charge transport kinetics in the electrocatalysis (38, 39). Over Cu catalysts, the electrochemical reduction products of CO_2 highly depend on their exposed planes, valence states, and surface species (13, 18, 22, 23). CO adsorbs on metallic Cu (111) much weaker than on many catalytic metals such as Pt, Pd, Ni, and Ru (40–42), similar to the situation on Au and Ag. We thus attribute the high selectivity toward CO by the Cu/Ni(OH)₂ nanosheets to their excellent stability in maintaining the metallic nature of Cu components within the nanosheets during electrocatalysis due to the stabilizing effect by surface formate, thus preventing the further adsorption and reduction of CO on the catalyst.

DISCUSSION
Here, a unique synthetic strategy has been developed to prepare ultrastable hybrid Cu/Ni(OH)₂ nanosheets. A series of analytical methods have been used to study the fabrication, detailed structure and formation mechanism, stability, and catalytic performance in energy conversion of the unique Cu-based ultrathin nanosheets. Together with their major exposure surface of Cu (111), the enhanced stability of

Cu nanosheets by formate against oxidation explained why only CO was yielded in the electrochemical reduction of CO_2 on the hybrid Cu/Ni(OH)₂ nanosheets, making these air-stable Cu nanosheets behave like Au and Ag in the electroreduction of CO_2. With only CO yielded as the reduction product of CO_2 under low overpotentials, the hybrid Cu/Ni(OH)₂ nanosheets reported in this work serve as an ideal electrocatalyst for the electrochemical production of tunable syngas from CO_2 and H_2O by applying different potentials. The work also demonstrates the importance of surface coordination chemistry in determining the chemical properties of metal nanomaterials (43).

MATERIALS AND METHODS
Materials
Nickel chloride (NiCl₂), copper acetylacetonate [Cu(acac)₂], sodium formate (HCOONa), DMF, formic acid (HCOOH), acetone, and ethanol were used. All reagents were purchased from Sinopharm Chemical Reagent Co. Ltd. The ultrapure water used in all experiments with a resistivity of 18.2 megohms was prepared using an ultrapure water system.

Preparation of ultrathin hybrid Cu/Ni(OH)₂ nanosheets
In a typical synthesis, 50 mg of NiCl₂, 50 mg of Cu(acac)₂, and 100 mg of HCOONa were dissolved in 10 ml of DMF to form a homogeneous solution. The mixture was sealed in a 50-ml glass pressure vessel. The

mixture was then heated from room temperature to 160°C in 30 min and kept at 160°C for 10 hours. The maroon products were collected and rinsed three times with deionized water.

Preparation of Cu nanosheets
In a typical synthesis, 50 mg of Cu/Ni(OH)$_2$ nanosheets, 10 ml of HCOOH, 50 mg of HCOONa were dissolved in 40 ml of deionized water, and the mixture was stirred under nitrogen for 5 days at room temperature. The maroon products were collected and rinsed three times with deionized water.

Preparation of Cu nanoparticles
In a typical synthesis, 50 mg of Cu(acac)$_2$ and 100 mg of HCOONa were dissolved in 10 ml of DMF to form a homogeneous solution. The mixture was sealed in a 50-ml glass pressure vessel. The mixture was then heated from room temperature to 160°C in 30 min and kept at 160°C for 20 hours. The maroon products were collected and rinsed three times with deionized water.

Preparation of ultrathin α-Ni(OH)$_2$ nanosheets
In a typical synthesis, 50 mg of NiCl$_2$ and 100 mg of HCOONa were dissolved in 10 ml of DMF to form a homogeneous solution. The mixture was sealed in a 50-ml glass pressure vessel and heated at 120°C for 5 hours. The light green products were collected and rinsed three times with deionized water.

Preparation of ultrathin β-Ni(OH)$_2$ hexagonal nanosheets
The preparation of β-Ni(OH)$_2$ hexagonal nanosheets followed the reported method in the study by Gao et al. (44). In a typical synthesis, 100 mg of NiCl$_2$ was added into 20 ml of water to form a homogeneous solution. Then, 1 ml of oleylamine and 2 ml of ethanol were quickly added, and the mixture was stirred for 0.5 hours under ambient condition to form a homogenous solution. The mixture was sealed in a 50-ml glass pressure vessel and heated at 160°C for 10 hours. The resulting green products was collected and washed with cyclohexane, distilled water, and ethanol.

Preparation of ultrathin Cu/α-Ni(OH)$_2$ nanosheets by two steps
In a typical synthesis, 20 mg of α-Ni(OH)$_2$ nanosheets, 50 mg of Cu(acac)$_2$, and 100 mg of HCOONa were dissolved in 10 ml of DMF to form a homogeneous solution. The mixture was sealed in a 50-ml glass pressure vessel. The mixture was then heated from room temperature to 160°C in 30 min and kept at 160°C for 10 hours. The maroon products were collected and rinsed three times with deionized water.

Preparation of Cu/β-Ni(OH)$_2$ nanosheets by two steps
In a typical synthesis, 20 mg of β-Ni(OH)$_2$ nanosheets, 50 mg of Cu(acac)$_2$, and 100 mg of HCOONa were dissolved in 10 ml of DMF to form a homogeneous solution. The mixture was sealed in a 50-ml glass pressure vessel. The mixture was then heated from room temperature to 160°C in 30 min and kept at 160°C for 10 hours. The maroon products were collected and rinsed three times with deionized water.

Characterizations
TEM investigation was carried out using an HRTEM (JEM-2100F, JEOL) operated at 200 kV and Tecnai F-30 operated at 300 kV. All samples were dispersed in absolute ethanol solution and then dropped

on a Mo grid. AFM in the present work was performed using a Veeco DI NanoScope MultiMode V system.

Phase purity of the sample was characterized by XRD (D/max 2550VL/PC) with Cu Kα radiation from 10° to 80° at a scanning rate of 4°/min. The x-ray tube voltage and current were set at 35 kV and 200 mA, respectively. UV-vis absorption spectra were recorded on a Varian Cary 5000 spectrophotometer.

HS-LEISS measurements were carried out on an Ion-TOF Qtac 100 LEIS analyzer. Ar$^+$ ions with a kinetic energy of 5 keV were applied at a low ion flux of 1600 pA/cm^2.

The scattering angle was 145°. The IR spectra of the solid samples were recorded from 4000 to 400 cm^{-1} on a Nicolet 380 FTIR spectrometer (Thermo Electron Corporation) using KBr pellets.

Elemental analysis was performed on a Vario ELIII. The surface topography and thickness of nanofilms were viewed on an environment control scanning probe microscope (SII NanoNavi E-Sweep), in which the longitudinal and lateral resolutions were 0.03 and 1 nm, respectively.

The x-ray absorption spectra at the Cu K-edge and Ni K-edge were recorded at room temperature in transmission mode using ion chambers at the beamline BL14W1 of the Shanghai Synchrotron Radiation Facility, China. The photon energy was calibrated with the first inflection point of Cu K-edge in the Cu metal foil. The resulting XAS data were processed using WinXAS version 3.11. The χ(k) data were weighted by k^2 and Fourier-transformed to R-space (the k-space is 12 Å) to isolate the EXAFS contributions from each coordination shell. Reliable parameter values, such as bond distances, coordination numbers, etc., were determined via multiple-shell R-space fitting of Cu spectra.

XPS data were acquired using a Kratos Axis Ultra XPS incorporated with a 165-mm hemispherical electron energy analyzer. The incident radiation was monochromatic Al Kα x-rays at 150 W. Survey (wide) scans were taken at an analyzer pass energy of 160 eV and multiplex (narrow) high-resolution scans of Cu 2p and Ni 2p at a pass energy of 40 eV. Survey scans were carried out over 1200-eV binding energy range with 1.0-eV steps and a dwell time of 100 ms. Narrow high-resolution scans were run with 0.1-eV steps and 162-ms dwell time.

TPD-MS measurement was carried out in an in situ pyrolysis TPD-MS apparatus. The samples were heated from room temperature to 650°C with a heating rate of 5°C/min. The mass spectrum and sample temperature were recorded simultaneously. Each spectrum is an accumulation of 1000 spectra gathered at an interval of 100 μs. The typical pressure of the pyrolytic furnace is kept at 2 × 10^{-4} Pa to prevent secondary reactions.

Electrochemical measurements
All electrochemical properties were investigated on a CHI 760e electrochemical workstation in a three-electrode configuration cell using as-prepared sample loading on carbon paper as the working electrode, platinum plate (1 × 1 cm^2) as the counter electrode, and SCE as the reference electrode in 0.5 M NaHCO$_3$ aqueous electrolyte (pH 7.2), whereas the active area was precisely controlled at 1 × 1 cm^2. CO$_2$ RR polarization curves were collected at a scan rate of 10 mV/s. The scheme of the electrocatalysis setup is shown in fig. S33. All the electrolyses were conducted in a working compartment containing 20 ml of the electrolyte with gas headspace of 5 ml. The anode and cathode compartments of the electrochemical cell were separated by a Nafion membrane. Before the measurement, the working electrode compartment was purged with CO$_2$ for 20 min to prepare CO$_2$-saturated electrolyte and the flow rate of 15 ml/min. During chronoamperometry,

gas products from the cell went through the sampling loop of a gas chromatograph. The gas products were analyzed by a TCD (thermal conductivity detector) for H_2 and an FID (flame ionization detector) for CO and hydrocarbons. The gas-phase product was sampled every 30 min using a gas-tight syringe. The gas chromatograph (GC-2014, Shimadzu) equipped with PLOT Mol Sieve 5A and Q-bond PLOT columns was used for quantifications. Ar (99.999%) was used as the carrier gas. Liquid products were analyzed by ^1H NMR spectra, which were recorded on an Advance III 500-MHz Unity plus spectrometer (Bruker), in which 0.5 ml of the electrolyte was mixed with 0.1 ml of D_2O (deuterated water) and 0.015 μl of dimethyl sulfoxide (DMSO) (99.99%, Sigma) was added as an internal standard. In all the ^1H NMR spectra, the singlet at a chemical shift of 2.54 parts per million corresponded to DMSO. The Nyquist plots were measured with frequencies ranging from 100 kHz to 0.1 Hz, and the amplitude of the applied voltage was 1 mV. The impedance data were fitted to a simplified Randles circuit to extract the charge-transfer resistances. In all measurements, we used SCE as the reference. It was calibrated with respect to RHE. In 0.5 M $NaHCO_3$, E (RHE) = E (SCE) + 0.2412 + pH × 0.0592 = E (SCE) + 0.667. Overpotential (V) = E (RHE) − E_0 (CO_2/CO). E_0 (CO_2/CO) is the reduction potential for CO_2/CO (−0.11 V versus RHE). All the electrolyses were conducted at room temperature, and 80% IR correction was applied in all measurements.

SUPPLEMENTARY MATERIALS

Supplementary material for this article is available at http://advances.sciencemag.org/cgi/content/full/3/9/e1701069/DC1

fig. S1. Large-scale SEM and TEM images and SAED pattern of the Cu/Ni(OH)₂ nanosheets.
fig. S2. EDX spectrum of the Cu/Ni(OH)₂ nanosheets.
fig. S3. UV-vis absorption spectrum of the dispersion of the Cu/Ni(OH)₂ nanosheets in ethanol.
fig. S4. STEM and EDX mapping images of the Cu/Ni(OH)₂ nanosheets.
fig. S5. XPS spectra of the Cu/Ni(OH)₂ nanosheets.
fig. S6. Experimental FT-EXAFS spectrum and the best fits of the as-prepared Cu/Ni(OH)₂ nanosheets and Cu foil.
fig. S7. Three structural models of Cu to simulate their FT-EXAFS using the FEFF 8 program: bulk Cu, two-atomic-layer Cu, and one-atomic-layer Cu.
fig. S8. TEM, AFM, XRD, and XPS characterizations of the Cu nanosheets.
fig. S9. TEM images of the products obtained with the different heating time at 160°C.
fig. S10. XRD patterns of the products obtained with the different heating time at 160°C: 0, 1, 3, 5, and 15 hours.
fig. S11. Relative contents of Cu and Ni in the products obtained with different heating time at 160°C.
fig. S12. TEM images and XRD patterns of the products obtained at different hydrothermal temperatures.
fig. S13. Two possible pathways for the deposition of Cu²⁺ onto premade Ni(OH)₂ nanosheets subsequent deposition with Cu(OH)₂ continually grown on Ni(OH)₂ (pathway I) and substitution deposition (pathway II) with surface Ni²⁺ replaced by Cu²⁺.
fig. S14. TEM and AFM images of Ni(OH)₂ nanosheets before and after Cu²⁺ substitution, and HS-LEISS spectra for Cu(OH)₂/Ni(OH)₂ nanosheets.
fig. S15. TEM, XRD, and EDX characterizations of Cu₂O intermediates and Cu nanosheets using β-Ni(OH)₂ as the template.
fig. S16. TEM images and XRD of the α-Ni(OH)₂ and Cu/α-Ni(OH)₂ nanosheets.
fig. S17. TEM and HR-TEM images and XRD pattern of the Cu nanoparticles synthesized in the absence of Ni.
fig. S18. TEM image of the Cu/Ni(OH)₂ nanosheets after being heated at 280°C in N₂ for 3 hours.
fig. S19. XPS and Auger electron spectra of the Cu/Ni(OH)₂ nanosheets after storing in air at room temperatures for 90 days.
fig. S20. Thermal stability of the hybrid Cu/Ni(OH)₂ nanosheets at 100°C in air.
fig. S21. N₂ adsorption isotherm of the Cu/Ni(OH)₂ nanosheets at 77 K.
fig. S22. Effect of surface formate modification on the stability of Cu foils against oxidation.
fig. S23. Air instability of the Cu/Ni(OH)₂ nanosheets after surface ligand exchange by acetate.
fig. S24. TPD-MS profiles of the species released from the acetate-exchanged Cu/Ni(OH)₂ nanosheets under the TPD-MS measuring condition.
fig. S25. Photograph of the reaction mixture without the addition of HCOONa after being heated at the same conditions as those for the synthesis of the Cu/Ni(OH)₂ nanosheets.
fig. S26. Electrocatalytic performances of pure Cu nanoparticles and Ni(OH)₂ nanosheets in the CO₂ reduction.
fig. S27. ¹H NMR spectra of products after bulk electrolysis at different potentials for 2 hours on the Cu/Ni(OH)₂ nanosheets modified carbon paper electrode.
fig. S28. TEM image and electrocatalytic performance of the Cu nanosheets in CO₂ reduction.
fig. S29. Loading-dependent chronoamperometric currents at −0.5 V versus RHE.
fig. S30. TEM images of the Cu and Cu/Ni(OH)₂ nanosheets after electrochemical tests.
fig. S31. Room-temperature CO₂ adsorption isotherms of the Cu/Ni(OH)₂ nanosheets, Cu nanosheets obtained from the Cu/Ni(OH)₂ nanosheets by etching away Ni(OH)₂, Cu nanoparticles made with the same conditions of Cu/Ni(OH)₂ except that no Ni was introduced, and Ni(OH)₂ nanosheets prepared with the same conditions of Cu/Ni(OH)₂ except that no Cu was introduced.
fig. S32. Nyquist plots of the four different samples under the potential of −0.5 V (versus RHE).
fig. S33. Scheme of the setup for the electrochemical reduction of CO₂.
table S1. EXAFS parameters of the Cu foil and Cu/Ni(OH)₂ nanosheets.
table S2. The elemental analysis results of two different Cu/Ni(OH)₂ nanosheets.

REFERENCES AND NOTES

1. F. Jiao, J. Li, X. Pan, J. Xiao, H. Li, H. Ma, M. Wei, Y. Pan, Z. Zhou, M. Li, S. Miao, J. Li, Y. Zhu, D. Xiao, T. He, J. Yang, F. Qi, Q. Fu, X. Bao, Selective conversion of syngas to light olefins. *Science* **351**, 1065–1068 (2016).
2. C. W. Li, J. Ciston, M. W. Kanan, Electroreduction of carbon monoxide to liquid fuel on oxide-derived nanocrystalline copper. *Nature* **508**, 504–507 (2014).
3. G. A. Olah, A. Molnar, G. K. Surya Prakash, *Hydrocarbon Chemistry* (John Wiley & Sons, 2003).
4. L. Zhong, F. Yu, Y. An, Y. Zhao, Y. Sun, Z. Li, T. Lin, Y. Lin, X. Qi, Y. Dai, L. Gu, J. Hu, S. Jin, Q. Shen, H. Wang, Cobalt carbide nanoprisms for direct production of lower olefins from syngas. *Nature* **538**, 84–87 (2016).
5. D. A. Hickman, L. D. Schmidt, Production of syngas by direct catalytic oxidation of methane. *Science* **259**, 343–346 (1993).
6. D. J. Wilhelm, D. R. Simbeck, A. D. Karp, R. L. Dickenson, Syngas production for gas-to-liquids applications: Technologies, issues and outlook. *Fuel Process. Technol.* **71**, 139–148 (2001).
7. B. Kamm, Production of platform chemicals and synthesis gas from biomass. *Angew. Chem. Int. Ed.* **46**, 5056–5058 (2007).
8. J. R. Rostrup-Nielsen, New aspects of syngas production and use. *Catal. Today* **63**, 159–164 (2000).
9. J. Qiao, Y. Liu, F. Hong, J. Zhang, A review of catalysts for the electroreduction of carbon dioxide to produce low-carbon fuels. *Chem. Soc. Rev.* **43**, 631–675 (2014).
10. D. Kim, J. Resasco, Y. Yu, A. M. Asiri, P. Yang, Synergistic geometric and electronic effects for electrochemical reduction of carbon dioxide using gold–copper bimetallic nanoparticles. *Nat. Commun.* **5**, 4948 (2014).
11. Q. Lu, J. Rosen, Y. Zhou, G. S. Hutchings, Y. C. Kimmel, J. G. Chen, F. Jiao, A selective and efficient electrocatalyst for carbon dioxide reduction. *Nat. Commun.* **5**, 3242 (2014).
12. W. Sheng, S. Kattel, S. Yao, B. Yan, Z. Liang, C. J. Hawxhurst, Q. Wu, J. G. Chen, Electrochemical reduction of CO₂ to synthesis gas with controlled CO/H₂ ratios. *Energy Environ. Sci.* **10**, 1180–1185 (2017).
13. H. Mistry, A. S. Varela, S. Kühl, P. Strasser, B. R. Cuenya, Nanostructured electrocatalysts with tunable activity and selectivity. *Nat. Rev. Mater.* **1**, 16009 (2016).
14. R. Angamuthu, P. Byers, M. Lutz, A. L. Spek, E. Bouwman, Electrocatalytic CO₂ conversion to oxalate by a copper complex. *Science* **327**, 313–315 (2010).
15. S. Lin, C. S. Diercks, Y.-B. Zhang, N. Kornienko, E. M. Nichols, Y. Zhao, A. R. Paris, D. Kim, P. Yang, O. M. Yaghi, C. J. Chang, Covalent organic frameworks comprising cobalt porphyrins for catalytic CO₂ reduction in water. *Science* **349**, 1208–1213 (2015).
16. S. Gao, Y. Lin, X. Jiao, Y. Sun, Q. Luo, W. Zhang, D. Li, J. Yang, Y. Xie, Partially oxidized atomic cobalt layers for carbon dioxide electroreduction to liquid fuel. *Nature* **529**, 68–71 (2016).
17. Y. Li, F. Cui, M. B. Ross, D. Kim, Y. Sun, P. Yang, Structure-sensitive CO₂ electroreduction to hydrocarbons on ultrathin 5-fold twinned copper nanowires. *Nano Lett.* **17**, 1312–1317 (2017).
18. M. S. Xie, B. Y. Xia, Y. Li, Y. Yan, Y. Yang, Q. Sun, S. H. Chan, A. Fisher, X. Wang, Amino acid modified copper electrodes for the enhanced selective electroreduction of carbon dioxide towards hydrocarbons. *Energy Environ. Sci.* **9**, 1687–1695 (2016).
19. R. Reske, H. Mistry, F. Behafarid, B. Roldan Cuenya, P. Strasser, Particle size effects in the catalytic electroreduction of CO₂ on Cu nanoparticles. *J. Am. Chem. Soc.* **136**, 6978–6986 (2014).
20. D. Raciti, K. J. Livi, C. Wang, Highly dense Cu nanowires for low-overpotential CO₂ reduction. *Nano Lett.* **15**, 6829–6835 (2015).

21. A. Loiudice, P. Lobaccaro, E. A. Kamali, T. Thao, B. H. Huang, J. W. Ager, R. Buonsanti, Tailoring copper nanocrystals towards C_2 products in electrochemical CO_2 reduction. *Angew. Chem. Int. Ed.* **55**, 5789–5792 (2016).

22. M. Ma, K. Djanashvili, W. A. Smith, Controllable hydrocarbon formation from the electrochemical reduction of CO_2 over Cu nanowire arrays. *Angew. Chem. Int. Ed.* **128**, 6792–6796 (2016).

23. C. W. Li, M. W. Kanan, CO_2 reduction at low overpotential on Cu electrodes resulting from the reduction of thick Cu_2O films. *J. Am. Chem. Soc.* **134**, 7231–7234 (2012).

24. S. Zhang, P. Kang, T. J. Meyer, Nanostructured tin catalysts for selective electrochemical reduction of carbon dioxide to formate. *J. Am. Chem. Soc.* **136**, 1734–1737 (2014).

25. F. Lei, W. Liu, Y. Sun, J. Xu, K. Liu, L. Liang, T. Yao, B. Pan, S. Wei, Y. Xie, Metallic tin quantum sheets confined in graphene toward high-efficiency carbon dioxide electroreduction. *Nat. Commun.* **7**, 12697 (2016).

26. M. Asadi, K. Kim, C. Liu, A. V. Addepalli, P. Abbasi, P. Yasaei, P. Phillips, A. Behranginia, J. M. Cerrato, R. Haasch, P. Zapol, B. Kumar, R. F. Klie, J. Abiade, L. A. Curtiss, A. Salehi-Khojin, Nanostructured transition metal dichalcogenide electrocatalysts for CO_2 reduction in ionic liquid. *Science* **353**, 467–470 (2016).

27. Y. Chen, C. W. Li, M. W. Kanan, Aqueous CO_2 reduction at very low overpotential on oxide-derived Au nanoparticles. *J. Am. Chem. Soc.* **134**, 19969–19972 (2012).

28. M. B. Gawande, A. Goswami, F.-X. Felpin, T. Asefa, X. Huang, R. Silva, X. Zou, R. Zboril, R. S. Varma, Cu and Cu-based nanoparticles: Synthesis and applications in catalysis. *Chem. Rev.* **116**, 3722–3811 (2016).

29. M. Jin, G. He, H. Zhang, J. Zeng, Z. Xie, Y. Xia, Shape-controlled synthesis of copper nanocrystals in an aqueous solution with glucose as a reducing agent and hexadecylamine as a capping agent. *Angew. Chem. Int. Ed.* **50**, 10560–10564 (2011).

30. L. Xu, Y. Yang, Z.-W. Hu, S.-H. Yu, Comparison study on the stability of copper nanowires and their oxidation kinetics in gas and liquid. *ACS Nano* **10**, 3823–3834 (2016).

31. H.-J. Yang, S.-Y. He, H.-L. Chen, H.-Y. Tuan, Monodisperse copper nanocubes: Synthesis, self-assembly, and large-area dense-packed films. *Chem. Mater.* **26**, 1785–1793 (2014).

32. Z.-J. Zuo, J. Li, P.-D. Han, W. Huang, XPS and DFT studies on the autoxidation process of Cu sheet at room temperature. *J. Phys. Chem. C* **118**, 20332–20345 (2014).

33. Y. Tang, C. A. Roberts, R. T. Perkins, I. E. Wachs, Revisiting formic acid decomposition on metallic powder catalysts: Exploding the HCOOH decomposition volcano curve. *Surf. Sci.* **650**, 103–110 (2016).

34. B. E. Hayden, K. Prince, D. P. Woodruff, A. M. Bradshaw, An iras study of formic acid and surface formate adsorbed on Cu(110). *Surf. Sci.* **133**, 589–604 (1983).

35. E. M. Nichols, J. J. Gallagher, C. Liu, Y. Su, J. Resasco, Y. Yu, Y. Sun, P. Yang, M. C. Y. Chang, C. J. Chang, Hybrid bioinorganic approach to solar-to-chemical conversion. *Proc. Natl. Acad. Sci. U.S.A.* **112**, 11461–11466 (2015).

36. M. R. Singh, E. L. Clark, A. T. Bell, Thermodynamic and achievable efficiencies for solar-driven electrochemical reduction of carbon dioxide to transportation fuels. *Proc. Natl. Acad. Sci. U.S.A.* **112**, E6111–E6118 (2015).

37. C. Costentin, M. Drouet, M. Robert, J.-M. Savéant, A local proton source enhances CO_2 electroreduction to CO by a molecular Fe catalyst. *Science* **338**, 90–94 (2012).

38. J. Bao, X. Zhang, B. Fan, J. Zhang, M. Zhou, W. Yang, X. Hu, H. Wang, B. Pan, Y. Xie, Ultrathin spinel-structured nanosheets rich in oxygen deficiencies for enhanced electrocatalytic water oxidation. *Angew. Chem. Int. Ed.* **54**, 7399–7404 (2015).

39. L. Dai, Q. Qin, X. Zhao, C. Xu, C. Hu, S. Mo, Y. O. Wang, S. Lin, Z. Tang, N. Zheng, Electrochemical partial reforming of ethanol into ethyl acetate using ultrathin Co_3O_4 nanosheets as a highly selective anode catalyst. *ACS Cent. Sci.* **2**, 538–544 (2016).

40. K. J. Andersson, F. Calle-Vallejo, J. Rossmeisl, I. Chorkendorff, Adsorption-driven surface segregation of the less reactive alloy component. *J. Am. Chem. Soc.* **131**, 2404–2407 (2009).

41. B. Hammer, Y. Morikawa, J. K. Nørskov, CO chemisorption at metal surfaces and overlayers. *Phys. Rev. Lett.* **76**, 2141–2144 (1996).

42. Z. Zhang, Z. Luo, B. Chen, C. Wei, J. Zhao, J. Chen, X. Zhang, Z. Lai, Z. Fan, C. Tan, M. Zhao, Q. Lu, B. Li, Y. Zong, C. Yan, G. Wang, Z. J. Xu, H. Zhang, One-pot synthesis of highly anisotropic five-fold-twinned PtCu nanoframes used as a bifunctional electrocatalyst for oxygen reduction and methanol oxidation. *Adv. Mater.* **28**, 8712–8717 (2016).

43. P. Liu, R. Qin, G. Fu, N. Zheng, Surface coordination chemistry of metal nanomaterials. *J. Am. Chem. Soc.* **139**, 2122–2131 (2017).

44. M. Gao, W. Sheng, Z. Zhuang, Q. Fang, S. Gu, J. Jiang, Y. Yan, Efficient water oxidation using nanostructured α-nickel-hydroxide as an electrocatalyst. *J. Am. Chem. Soc.* **136**, 7077–7084 (2014).

Citation: L. Dai, Q. Qin, P. Wang, X. Zhao, C. Hu, P. Liu, R. Qin, M. Chen, D. Ou, C. Xu, S. Mo, B. Wu, G. Fu, P. Zhang, N. Zheng, Ultrastable atomic copper nanosheets for selective electrochemical reduction of carbon dioxide. *Sci. Adv.* **3**, e1701069 (2017).

Science Advances

Ultrastable atomic copper nanosheets for selective electrochemical reduction of carbon dioxide

Lei Dai, Qing Qin, Pei Wang, Xiaojing Zhao, Chengyi Hu, Pengxin Liu, Ruixuan Qin, Mei Chen, Daohui Ou, Chaofa Xu, Shiguang Mo, Binghui Wu, Gang Fu, Peng Zhang and Nanfeng Zheng

ARTICLE TOOLS	http://advances.sciencemag.org/content/3/9/e1701069
SUPPLEMENTARY MATERIALS	http://advances.sciencemag.org/content/suppl/2017/09/01/3.9.e1701069.DC1
REFERENCES	This article cites 43 articles, 8 of which you can access for free http://advances.sciencemag.org/content/3/9/e1701069#BIBL
PERMISSIONS	http://www.sciencemag.org/help/reprints-and-permissions

Use of this article is subject to the Terms of Service